SUPPLEMENTARY MATERIALS

Theoretical model for the optoacoustic continuum system

Backward Brillouin anti-Stokes scattering in a typical optical waveguide is an optoacoustic interaction between an optical pump wave, a scattered optical anti-Stokes wave, and an acoustic wave. The dynamics of this optoacoustic interaction can be given by

$$\begin{aligned}\frac{\partial a_{\mathrm{p}}}{\partial t}+\upsilon_{\mathrm{opt}}\frac{\partial a_{\mathrm{p}}}{\partial z}&=-\frac{\gamma_{\mathrm{opt}}}{2}a_{\mathrm{p}}-ig_0a_{\mathrm{aS}}^{\dagger}b_{\mathrm{ac}}+\sqrt{\gamma_{\mathrm{opt}}}\xi_{\mathrm{p}},\\ \frac{\partial a_{\mathrm{aS}}}{\partial t}-\upsilon_{\mathrm{opt}}\frac{\partial a_{\mathrm{aS}}}{\partial z}&=-\frac{\gamma_{\mathrm{opt}}}{2}a_{\mathrm{aS}}-ig_0a_{\mathrm{p}}b_{\mathrm{ac}}+\sqrt{\gamma_{\mathrm{opt}}}\xi_{\mathrm{aS}},\\ \frac{\partial b_{\mathrm{ac}}}{\partial t}-\upsilon_{\mathrm{ac}}\frac{\partial b_{\mathrm{ac}}}{\partial z}&=-\frac{\Gamma_{\mathrm{m}}}{2}b_{\mathrm{ac}}-ig_0a_{\mathrm{p}}^{\dagger}a_{\mathrm{aS}}+\sqrt{\Gamma_{\mathrm{m}}}\xi_{\mathrm{ac}},\end{aligned}\tag{5}$$

where $a_{\mathrm{p}}(z,t)$, $a_{\mathrm{aS}}(z,t)$, and $b_{\mathrm{ac}}(z,t)$ correspond to the envelope bosonic operators of the pump, anti-Stokes, and acoustic waves. γ_{opt} (Γ_{m}) and υ_{opt} (υ_{ac}) denote the linewidth and group velocity for the optical (acoustic) wave, respectively. g_0 is the vacuum coupling strength. ξ_{p}, ξ_{aS}, and ξ_{ac} are quantum Langevin noises corresponding to these three waves, which obey the following statistical properties

$$\begin{aligned}\langle\xi_{\mathrm{p}}(t,z)\rangle&=\langle\xi_{\mathrm{aS}}(t,z)=\langle\xi_{\mathrm{ac}}(t,z)=0,\\ \langle\xi_{\mathrm{p}}^{\dagger}(t_1,z_1)\xi_{\mathrm{p}}(t_2,z_2)\rangle&=\langle\xi_{\mathrm{aS}}^{\dagger}(t_1,z_1)\xi_{\mathrm{aS}}(t_2,z_2)\rangle=0,\\ \langle\xi_{\mathrm{ac}}^{\dagger}(t_1,z_1)\xi_{\mathrm{ac}}(t_2,z_2)\rangle&=n_{\mathrm{th}}\delta(t_1-t_2)\delta(z_1-z_2),\end{aligned}\tag{6}$$

where $n_{\mathrm{th}}=1/(e^{\hbar\Omega_{\mathrm{ac}}/k_{\mathrm{B}}T}-1)$ denotes the thermal phonon occupation of the acoustic wave at temperature T. In the undepleted pump regime where the reduction of pump power can be ignored, the three-wave interaction can be reduced a linearized beamsplitter interaction between anti-Stokes photons and acoustic phonons with an effective pump-enhanced coupling strength $g_{\mathrm{om}}=g_0\sqrt{\langle a_{\mathrm{p}}^{\dagger}a_{\mathrm{p}}\rangle}$. Therefore, the dynamics of the linearized optoacoustic interaction can be expressed as follows

$$\begin{aligned}\frac{\partial a_{\mathrm{aS}}}{\partial t}-\upsilon_{\mathrm{opt}}\frac{\partial a_{\mathrm{aS}}}{\partial z}&=-\frac{\gamma_{\mathrm{opt}}}{2}a_{\mathrm{aS}}-ig_{\mathrm{om}}b_{\mathrm{ac}}+\sqrt{\gamma_{\mathrm{opt}}}\xi_{\mathrm{aS}},\\ \frac{\partial b_{\mathrm{ac}}}{\partial t}-\upsilon_{\mathrm{ac}}\frac{\partial b_{\mathrm{ac}}}{\partial z}&=-\frac{\Gamma_{\mathrm{m}}}{2}b_{\mathrm{ac}}-ig_{\mathrm{om}}a_{\mathrm{aS}}+\sqrt{\Gamma_{\mathrm{m}}}\xi_{\mathrm{ac}}.\end{aligned}\tag{7}$$

Without the cavity structure, the optical anti-Stokes and acoustic waves contains continuously accessible groups of optical photons and acoustic phonons, respectively, i.e., envelope bosonic operators $a_{\mathrm{aS}}(z,t)$ and $b_{\mathrm{ac}}(z,t)$ at position z along the 1D waveguide can be constructed as

$$a_{\mathrm{aS}}(z,t)=\frac{1}{2\pi}\int dk\ a(k,t)e^{-ikz},\quad b_{\mathrm{ac}}(z,t)=\frac{1}{2\pi}\int dk\ b(k,t)e^{-ikz},\tag{8}$$

where $a(k,t)$ and $b(k,t)$ are annihilation operators for the k-th Stoke photon mode and acoustic phonon mode with wave number k. Moving into momentum space, Eq. (7) can be rewritten as

$$\begin{aligned}\frac{da(k,t)}{dt}&=\left(-\frac{\gamma_{\mathrm{opt}}}{2}+i\Delta_{\mathrm{as}}\right)a-ig_{\mathrm{om}}b+\sqrt{\gamma_{\mathrm{opt}}}\xi_a,\\ \frac{db(k,t)}{dt}&=\left(-\frac{\Gamma_{\mathrm{m}}}{2}+i\Delta_{\mathrm{ac}}\right)b-ig_{\mathrm{om}}a+\sqrt{\Gamma_{\mathrm{m}}}\xi_b,\end{aligned}\tag{9}$$

where k is the wave number in the momentum space. We can see that Eq. (9) describes a beamsplitter interaction between the k-th photon and phonon modes with interaction Hamiltonian $H_{\mathrm{int}}=\hbar g_{\mathrm{om}}(a^{\dagger}(k,t)b(k,t)+b^{\dagger}(k,t)a(k,t))$. Moving into the frequency domain via a Fourier transformation, Eq. (9) can be re-expressed as

$$\begin{aligned}-i\omega\tilde{a}(k,\omega)&=\left(-\frac{\gamma_{\mathrm{opt}}}{2}+i\Delta_{\mathrm{as}}\right)\tilde{a}(k,\omega)-ig_{\mathrm{om}}\tilde{b}(k,\omega)+\sqrt{\gamma_{\mathrm{opt}}}\tilde{\xi}_a(k,\omega),\\ -i\omega\tilde{b}(k,\omega)&=\left(-\frac{\Gamma_{\mathrm{m}}}{2}+i\Delta_{\mathrm{ac}}\right)\tilde{b}(k,\omega)-ig_{\mathrm{om}}\tilde{a}(k,\omega)+\sqrt{\Gamma_{\mathrm{m}}}\tilde{\xi}_b(k,\omega),\end{aligned}\tag{10}$$

where $\tilde{a}$, $\tilde{b}$, $\tilde{\xi}_a$, and $\tilde{\xi}_b$ correspond to the Fourier transform of a, b, ξ_a, and ξ_b. The solutions of above equations can be given by

$$\begin{aligned}
\tilde{a}(k,\omega) &= \frac{\left(\frac{\Gamma_{\mathrm{m}}}{2} - i(\omega+\Delta_{ac})\right)\sqrt{\gamma_{\mathrm{opt}}}\tilde{\xi}_a(\omega) - i g_{\mathrm{om}}\sqrt{\Gamma_{\mathrm{m}}}\tilde{\xi}_b(\omega)}{g_{\mathrm{om}}^2 + \left(\frac{\gamma_{\mathrm{opt}}}{2} - i(\omega+\Delta_{\mathrm{as}})\right)\left(\frac{\Gamma_{\mathrm{m}}}{2} - i(\omega+\Delta_{\mathrm{ac}})\right)}, \\
\tilde{b}(k,\omega) &= \frac{-i g_{\mathrm{om}}\sqrt{\gamma_{\mathrm{opt}}}\tilde{\xi}_a(\omega) + \left(\frac{\gamma_{\mathrm{opt}}}{2} - i(\omega+\Delta_{\mathrm{as}})\right)\sqrt{\Gamma_{\mathrm{m}}}\tilde{\xi}_b(\omega)}{g_{\mathrm{om}}^2 + \left(\frac{\gamma_{\mathrm{opt}}}{2} - i(\omega+\Delta_{\mathrm{as}})\right)\left(\frac{\Gamma_{\mathrm{m}}}{2} - i(\omega+\Delta_{\mathrm{ac}})\right)}.
\end{aligned} \tag{11}$$

We define the quadrature operators and the corresponding Fourier transform of anti-Stokes and acoustic modes as follows

$$\begin{aligned}
X_a(k,t) &= \frac{a^\dagger(k,t) + a(k,t)}{\sqrt{2}}, \quad Y_a(k,t) = \frac{a(k,t) - a^\dagger(k,t)}{\sqrt{2}i}, \\
\tilde{X}_b(k,t) &= \frac{\tilde{b}^\dagger(k,t) + \tilde{b}(k,t)}{\sqrt{2}}, \quad \tilde{Y}_b(k,t) = \frac{\tilde{b}^\dagger(k,t) - \tilde{b}(k,t)}{\sqrt{2}i}.
\end{aligned} \tag{12}$$

Thus we have

$$\langle \tilde{X}_a^\dagger(\omega_1)\tilde{X}_a(\omega_2)\rangle = 2\pi S_{XX}^{\mathrm{as}}(\omega_1)\delta(\omega_1-\omega_2), \tag{13}$$

where $S_{XX}^{\mathrm{as}}(k,\omega)$ denotes the displacement spectrum for the k-th anti-Stokes mode. Based on Eq. (6), the Langevin noises of $\tilde{\xi}_a$ and $\tilde{\xi}_b$ obey correlation relationships as follows

$$\begin{aligned}
&\langle \tilde{\xi}_a^\dagger(k,\omega_1)\tilde{\xi}_a(k,\omega_2)\rangle = 0, \\
&\langle \tilde{\xi}_a(k,\omega_1)\tilde{\xi}_a^\dagger(k,\omega_2)\rangle = 2\pi\delta(\omega_1-\omega_2), \\
&\langle \tilde{\xi}_b^\dagger(k,\omega_1)\tilde{\xi}_b(k,\omega_2)\rangle = 2\pi n_{\mathrm{th}}\delta(\omega_1-\omega_2), \\
&\langle \tilde{\xi}_b(k,\omega_1)\tilde{\xi}_b^\dagger(k,\omega_2)\rangle = 2\pi(n_{\mathrm{th}}+1)\delta(\omega_1-\omega_2).
\end{aligned} \tag{14}$$

According to noise correlations Eq. (14) and solution of anti-Stokes mode Eq. (11), we have

$$\begin{aligned}
\langle \tilde{a}^\dagger(\omega_1)\tilde{a}(\omega_2)\rangle &= \frac{2\pi g_{\mathrm{om}}^2\Gamma_{\mathrm{m}} n_{\mathrm{th}}\delta(\omega_1-\omega_2)}{\left|g_{\mathrm{om}}^2 + \left(\frac{\gamma_{\mathrm{opt}}}{2} + i(\omega_1+\Delta_{\mathrm{as}})\right)\left(\frac{\Gamma_{\mathrm{m}}}{2} + i(\omega_1+\Delta_{\mathrm{ac}})\right)\right|^2}, \\
\langle \tilde{a}(\omega_1)\tilde{a}^\dagger(\omega_2)\rangle &= 2\pi\frac{\gamma_{\mathrm{opt}}\left(\frac{\Gamma_{\mathrm{m}}^2}{4} + (\omega_1+\Delta_{\mathrm{ac}})^2\right) + g_{\mathrm{om}}^2\Gamma_{\mathrm{m}}(n_{\mathrm{th}}+1)}{\left|g_{\mathrm{om}}^2 + \left(\frac{\gamma_{\mathrm{opt}}}{2} + i(\omega_1+\Delta_{\mathrm{as}})\right)\left(\frac{\Gamma_{\mathrm{m}}}{2} + i(\omega_1+\Delta_{\mathrm{ac}})\right)\right|^2}\delta(\omega_1-\omega_2), \\
\langle \tilde{a}^\dagger(\omega_1)\tilde{a}^\dagger(\omega_2)\rangle &= 0, \\
\langle \tilde{a}(\omega_1)\tilde{a}(\omega_2)\rangle &= 0.
\end{aligned} \tag{15}$$

Thus we have

$$\begin{aligned}
&\langle \tilde{X}_a^\dagger(\omega_1)\tilde{X}_a(\omega_2)\rangle \\
&= \frac{\langle \tilde{a}^\dagger(\omega_1)\tilde{a}(\omega_2)\rangle + \langle \tilde{a}(\omega_1)\tilde{a}^\dagger(\omega_2)\rangle + \langle \tilde{a}^\dagger(\omega_1)\tilde{a}^\dagger(\omega_2)\rangle + \langle \tilde{a}(\omega_1)\tilde{a}(\omega_2)\rangle}{2} \\
&= 2\pi\frac{\frac{\gamma_{\mathrm{opt}}}{2}\left(\frac{\Gamma_{\mathrm{m}}}{2} + (\omega_1+\Delta_{\mathrm{ac}})^2\right) + \frac{\Gamma_{\mathrm{m}}}{2}g_{\mathrm{om}}^2(2n_{\mathrm{th}}+1)}{\left(g_{\mathrm{om}}^2 + \frac{\gamma_{\mathrm{opt}}\Gamma_{\mathrm{m}}}{4} - (\omega_1+\Delta_{\mathrm{as}})(\omega_1+\Delta_{\mathrm{ac}})\right)^2 + \frac{1}{4}\left(\gamma_{\mathrm{opt}}(\omega_1+\Delta_{\mathrm{ac}}) + \Gamma_{\mathrm{m}}(\omega_1+\Delta_{\mathrm{as}})\right)^2}\delta(\omega_1-\omega_2),
\end{aligned} \tag{16}$$

By comparing Eq. (13) and Eq. (16), the displacement spectrum of the k-th anti-Stokes mode can be given by

$$S_{XX}^{\mathrm{as}}(k,\omega) = \frac{\frac{\gamma_{\mathrm{opt}}}{2}\left(\frac{\Gamma_{\mathrm{m}}}{2} + (\omega+\Delta_{\mathrm{ac}})^2\right) + \frac{\Gamma_{\mathrm{m}}}{2}g_{\mathrm{om}}^2(2n_{\mathrm{th}}+1)}{\left(g_{\mathrm{om}}^2 + \frac{\gamma_{\mathrm{opt}}\Gamma_{\mathrm{m}}}{4} - (\omega+\Delta_{\mathrm{as}})(\omega+\Delta_{\mathrm{ac}})\right)^2 + \frac{1}{4}\left(\gamma_{\mathrm{opt}}(\omega+\Delta_{\mathrm{ac}}) + \Gamma_{\mathrm{m}}(\omega+\Delta_{\mathrm{as}})\right)^2}. \tag{17}$$

We show simulation results of spectra for anti-Stokes modes under the strong coupling regime in Fig. 5 (a) and (b). The dotted and dash-dot curves denote spectra of optical anti-Stokes modes for positive and negative wave number k, respectively. The black solid curve corresponds to the phase-matching case, i.e., $k = 0$. We can see that in the strong coupling regime, each anti-Stokes mode exhibits the normal-mode splitting. When the wave number k changes from

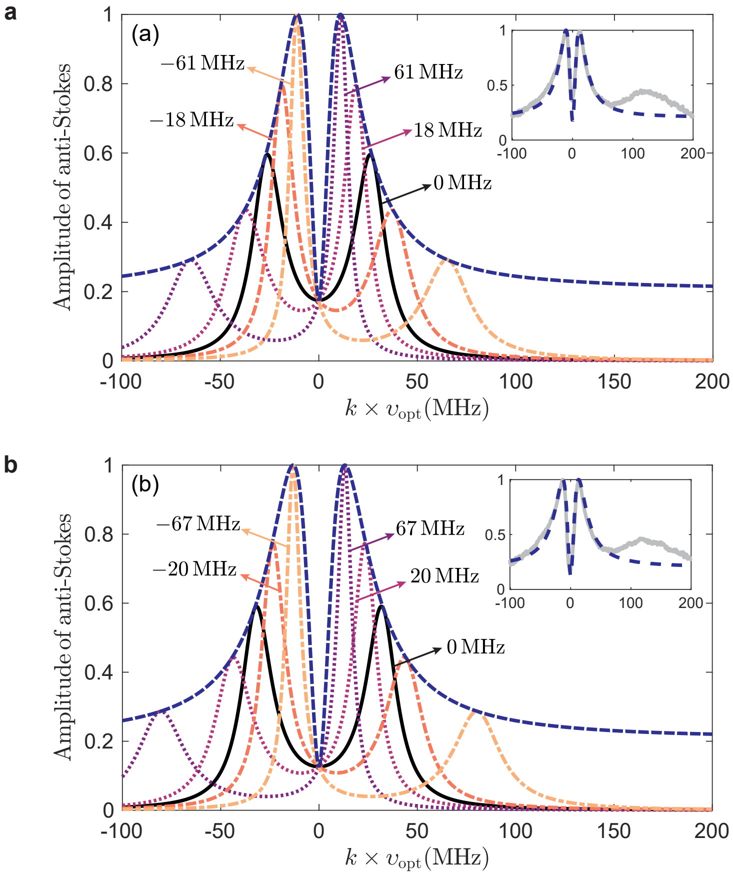

FIG. 5. **Simulation results of spectra for the anti-Stokes wave.** (a) The spectra of anti-Stokes wave with pump power of 0.83 W for various wave number k, where dotted (dash-dot) lines denote the spectrum of k-th anti-Stokes mode with positive (negative) wave number k and the black solid line correspond to the phase-matching case ($k = 0$). The dark blue dashed line shows the envelope of spectra for anti-Stokes modes with continuous wave number k. The inset indicates that experiment results (grey solid line) agree well with theoretical results (dark blue dashed line). (b) corresponds to the spectra of anti-Stokes wave with pump power of 1.21 W.

negative (dash-dot curves) to positive values (dotted curves), there is an avoided crossing, which is demonstrated in Fig. 3 in the main text. The insets in Fig. 5 (a) and (b) present the simulation (blue dashed curves) and experiment (red solid curves) results for different pump powers, which are in agreement with each other.

Similarly, the displacement spectrum for the k-th acoustic mode can be expressed as

$$S_{XX}^{\rm ac}(k,\omega) = \frac{\frac{\gamma_{\rm opt}}{2}\left(\frac{\Gamma_{\rm m}}{2} + (\omega+\Delta_{\rm ac})^2\right) + \frac{\Gamma_{\rm m}}{2} g_{\rm om}^2 (2n_{\rm th}+1)}{\left(g_{\rm om}^2 + \frac{\gamma_{\rm opt}\Gamma_{\rm m}}{4} - (\omega+\Delta_{\rm as})(\omega+\Delta_{\rm ac})\right)^2 + \frac{1}{4}\left(\gamma_{\rm opt}(\omega+\Delta_{\rm ac}) + \Gamma_{\rm m}(\omega+\Delta_{\rm as})\right)^2}. \tag{18}$$

The eigenvalues of coupled anti-Stokes and acoustic modes with wave number k can be given by

$$\omega_\pm = -\frac{\gamma_{\rm opt}+\Gamma_{\rm m}}{4} + i\frac{\Delta_{\rm as}+\Delta_{\rm ac}}{2} \pm i\sqrt{g_{\rm om}^2 - \left(\frac{\gamma_{\rm opt}-\Gamma_{\rm m}}{4} - i\frac{\Delta_{\rm as}-\Delta_{\rm ac}}{2}\right)^2}. \tag{19}$$

Sample

The sample used in the experiment is a 2.5 m highly nonlinear fiber (HNLF) placed inside a 4K Helium cryostat. The higher nonlinearity comes from the higher doping of Germanium in the core compared to single mode fiber (SMF). An HNLF has the same step-index, core-cladding structure as an SMF, allowing the sample to be spliced to standard

Table I. **Brillouin parameters for different samples.** Comparison of Brillouin parameters between room temperature standard SMF and the HNLF sample used in this study at room and cryogenic temperatures. These parameters are obtained for $\lambda_{\mathrm{pump}} = 1550$ nm. SMF parameters from [1].

Fiber type	Temperature (K)	Length (cm)	$\Omega_{\mathrm{B}}/2\pi$ (GHz)	Γ_{m} (MHz)	G_{B} ($\mathrm{W}^{-1}\mathrm{m}^{-1}$)	g_{B} ($\mathrm{W}^{-1}\mathrm{m}$)
SMF	293	-	10.87	20	0.14	$1.19 \cdot 10^{-11}$
HNLF	293	250	9.73	46.3	1.60	$8.1 \cdot 10^{-11}$
HNLF	4	150	9.60	9.91	6	$3.2 \cdot 10^{-10}$

APC connectors. The cladding and core diameters for both types of fiber is 125 µm and 8.2 µm [2], respectively. The loss of the sample in-coupling splice is -1.48 dB and of the out-coupling splice, -1.79 dB. In order to avoid heating because of the losses of the splices, these were placed outside of the cold plate of the cryostat, resulting in a cold section of the fiber estimated to be 1.5 m length. The parameters of the sample are given in Table I, comparing with standard SMF. The optical dissipation rate for this sample is $\gamma_{\mathrm{opt}} = 24 \pm 2$ MHz, where γ_{opt} is defined as

$$\gamma_{\mathrm{opt}} = \frac{\alpha_{\mathrm{linear}} c}{2\pi n}, \tag{20}$$

where c is the speed of light in vacuum, n the material refractive index and α_{linear} the linear loss.

Thermal-noise-initiated measurement

The setup used to perform a thermal-noise-initiated measurement via heterodyne detection is shown in Fig. 6. The continuous emission of a narrow line laser with a wavelength $\lambda_{\mathrm{pump}} = 1550$ nm is separated into two paths, pump and local oscillator (LO). The light in the pump arm is first amplified by a 5 W Erbium doped fiber amplifier (EDFA) and then filtered with a 0.8 nm tunable filter to remove the amplified spontaneous emission (ASE) coming from the EDFA. The pump is guided to the sample via a circulator, which redirects the back-reflected signal coming from the fiber into the detection part of the setup. As this signal will contain both the pump backreflection and the Brillouin resonance, a narrow-line tunable filter is used to selectively detect the Stokes or anti-Stokes signal. The leftover transmitted pump is dumped after the sample. An optical isolator is placed before the dump in order to reduce the back-reflected noise by 12 dB. Regarding the LO arm of the experiment, the frequency of the light is shifted 200 MHz by an acousto-optic modulator (AOM). This is allows to separate the two resonances in the detection device, which is particularly important for high pump power measurements in the cryostat. As the Stokes process enters the stimulated Brillouin-Mandelstam scattering (SBS) regime, the signal becomes so strong that it can not be fully filtered out. Frequency shifting the LO allows to measure the anti-Stokes signal without perturbations. The back-reflected signal and the LO are mixed in a 90:10 coupler and the interference directed to a high speed photodiode. A polarization controller in the LO arm is used to optimize the polarization overlap and therefore the signal. Finally, the transduced optical-into-electrical signal of the photodiode is sent and analyzed by an electrical spectrum analyzer (ESA).

The results for the experimental study of Brillouin-Mandelstam scattering in the sample at cryogenic temperatures are shown in Fig. 7 and Fig. 8 . As explained in the previous section, not the whole HNLF is at low temperature, as sections of it are outside of the base plate in order to allow splicing for optical access. This results in three regions of the fiber: cold, room temperature and transition between the two. This is reflected in the spectra shown in Fig. 7 (a). Two main peaks are present, the cold one centered at $\Omega_{\mathrm{B}}/2\pi = 9.5997 \pm 0.0001$ GHz and the room temperature one centered at $\Omega_{\mathrm{B}}/2\pi = 9.7278 \pm 0.0004$ GHz. As the pump power is increased, the cold Stokes resonance will enter the stimulated Brillouin-Mandelstam scattering regime (SBS), increasing exponentially and narrowing from 9.91 ± 0.07 MHz to 5.14 ± 0.04 MHz. On the contrary, the anti-Stokes resonance broadens until it splits in two, meaning the strong coupling regime has been reached (Fig. 8 (a)). Having a closer look at the cold part of the spectrum for low input power (Fig. 7 (b) and Fig. 8 (b)), two peaks of different linewidths centered around 9.5997 GHz are present. A narrow 9.91 MHz peak, corresponding to the cryogenic part of the sample, and a broader 77.2 ± 0.7 MHz peak. The source of this signal is the transition regions of the fiber, particularly of temperature around 190 K (Fig. 9 (a)). Around that temperature, the frequency shift is the same as at 4 K (Fig. 9 (b)), but the linewidth is higher (Fig. 9 (c)) [3].

The fact that these three regions of temperature are present in the sample is shown in Fig. 9 (a), where three peaks are present in the spectrum, the transition region one being the faintest because of the short length of fiber that generates it. The reason why there is a length of fiber at this specific temperature long enough to generate a distinct signal could be the following. Two parts of the fiber of approximately 1 cm each are adhered with silicone tape to the

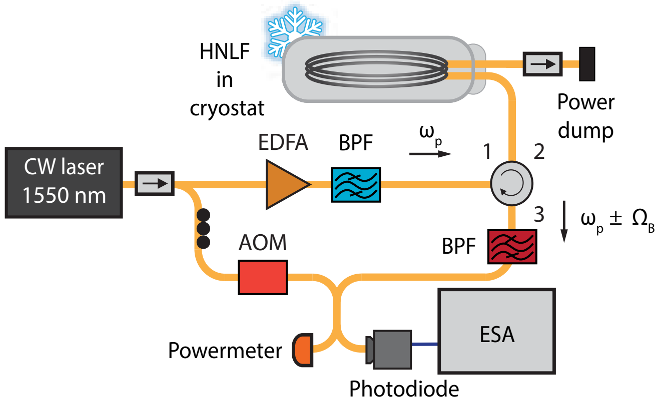

FIG. 6. **Thermal-noise-initiated experiment.** Diagram of the experimental setup used to measure thermal-noise-initiated Brillouin-Mandelstam scattering via heterodyne detection. CW: continuous wave; AOM: acousto-optical modulator; EDFA: erbium-doped fiber amplifier; BPF: band-pass filter, ESA: electrical spectrum analyzer. The three black circles represent a fiber polarization controller.

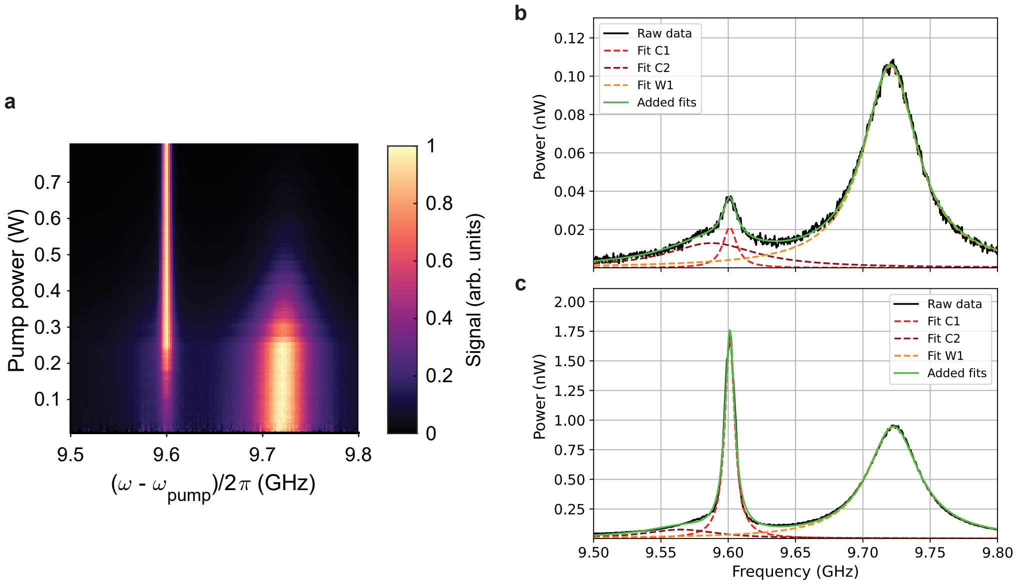

FIG. 7. **Thermal-noise-initiated measurement of Stokes resonances.** (a) Normalized Stokes Brillouin response of the sample as a function of pump power. As the pump power is increased, the resonance coming from the 4 K section (peak at 9.5997 GHz) enters the stimulated regime and increases exponentially. The response of the room temperature part (peak at 9.7278 GHz) is only visible for low powers, comparatively. (b) Spectrum of the full Stokes response of the sample at low input power. The signal centered at 9.6 GHz is composed of two peaks, a narrow 9.91 MHz one coming from the 4 K section of the fiber and a broad 77.2 MHz one coming from the transition to room temperature, at 190 K. (c) Spectrum of the full Stokes response of the sample at higher input power. The spectrum is now dominated by the narrow peak coming from the 4 K section of the fiber.

radiation shield of the cryostat, to which they are thermalized. As the rest of the fiber is suspended in vacuum, these are the only parts outside of a smooth temperature gradient. Given the short length of these sections, their response is only non-negligible at very low pump powers, in which the totality of the Brillouin response of the fiber comes from spontaneous scattering. As they are at a higher temperature than the cold part, more phonons are present there, allowing for a scattered signal to be measured. In order to calculate Γ_m correctly they need to be considered in the analysis. Nonetheless, for higher pump power, the response of the fiber at 9.5997 GHz mainly originates from the cold part of the fiber (Fig. 8 (c) and Fig. 7 (c)).

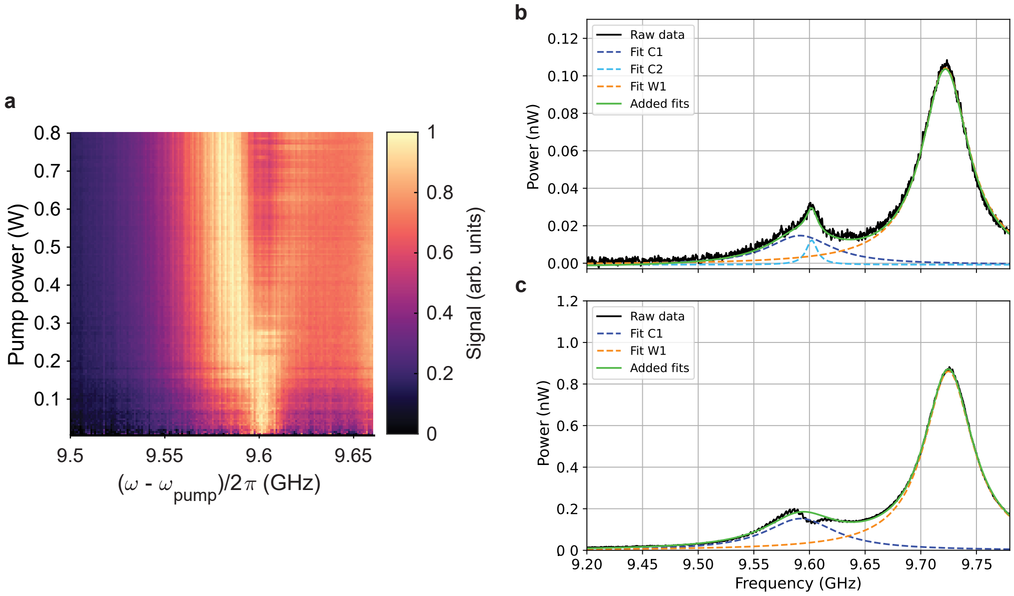

FIG. 8. **Thermal-noise-initiated measurement of anti-Stokes resonances.** (a) Normalized Anti-Stokes Brillouin response of the cryogenic sample as a function of pump power. As the pump power is increased, the resonance splits, corresponding to the transition into the strong coupling regime. (b) Spectrum of the full anti-Stokes response of the sample at low input power. Same behavior as described in 7 (b). (c) Spectrum of the full anti-Stokes response of the sample at higher input power. As the pump power increases, the signal coming from the 4 K region of the sample dominates the 9.6 GHz spectrum, showing the strong coupling splitting.

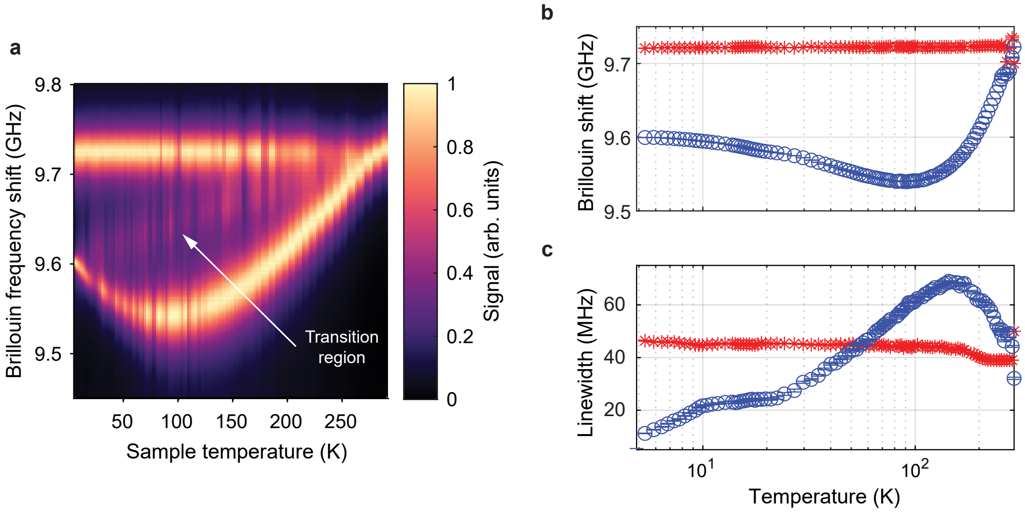

FIG. 9. **Stokes Brillouin response versus sample temperature.** (a) Stokes response of the sample as a function of sample temperature. The resonance at the top, centered at ($\Omega_B/2\pi = 9.72$ GHz), corresponds to the room temperature part of the fiber, and it does not shift as its temperature remains constant. On the lower part of the plot, the behavior of the sections of the fiber affected by the variation of temperature is shown. The most pronounced peak corresponds to the fiber section on the base plate of the cryostat. A faint third peak (indicated by the white arrow) is also present, coming from parts of the fiber in the transition. (b) Brillouin shift of two most prominent peaks as a function of sample temperature. The room temperature part of the fiber (red stars) is unaffected by the change in temperature. The temperature-varying peak (blue circles) crosses the 9.6 GHz point twice, at T = 191 K and at T = 4 K. (c) FWHM of the two most prominent peaks as a function of sample temperature. The room temperature part of the fiber (red stars) is unaffected by the change in temperature.

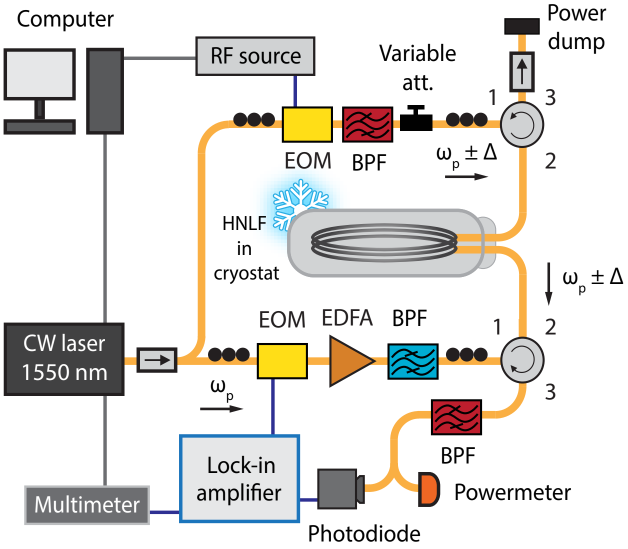

FIG. 10. **Pump-probe experiment.** Diagram of the setup used to measure Brillouin-Mandelstam scattering via a pump-probe experiment with lock-in amplifier detection. EOM: electro-optical modulator; Variable att.: variable attenuator; RF: radio frequency. The remaining abbreviations same as Fig. 6.

Pump-probe measurement

The setup used to perform the pump-probe experiment is shown in Fig. 10. The output of the laser described in the previous section is divided into two paths, pump and probe. The light of the pump arm is modulated by an electro-optical modulator (EOM) before amplification. The modulation frequency is given by a lock-in amplifier. The light of the probe arm is modulated by an EOM connected to an RF source, generating thus two sidebands $\omega_{\text{probe}} = \omega_{\text{pump}} \pm \Omega_{\text{B}} + \Delta_{\text{probe}}$. These sidebands are swept around the resonance frequency Ω_{B}. A narrowline bandpass filter is placed after the EOM to select one sideband and probe only one of the Brillouin processes. The light of each arm is coupled into the sample in opposite directions via circulators. To maximize the interaction between the different waves, polarization controllers are placed on each arm. The port 3 of the probe circulator is connected to an insulator followed by a power dump to get rid of the remaining pump light. The signal coming out of the port 3 of the pump circulator contains the probe frequency after the Brillouin interaction in the fiber plus the spontaneous scattering generated by the pump. To decrease the noise in the measurement, the back-reflection is filtered by a narrow bandpass filter. This signal is directed to a photodiode connected to the lock-in amplifier, where the resulting electrical signal is demodulated to obtain the probe power as a function of time. The amplified electrical output of the lock-in is measured by a multimeter. Both the RF-source and the multimeter are controlled by a computer, allowing to measure the resulting Brillouin spectrum after the sweep without the need of a frequency reference. It was not observed that the low power probe disturbs the strongly coupled system.

Temperature dependence of strong coupling threshold

As it was stated when describing the sample, we are able to reach the strong coupling regime thanks to the balance of losses, Brillouin gain and power handling in our platform. Working at cryogenic temperature is beneficial, as the acoustic dissipation rate (Γ_{m}) decreases significantly and the Brillouin gain G_{B}, on which the effective coupling strength depends, increases comparing to room temperature. Working at $T = 4$ K, the lowest temperature accessible in our experiment, proved to be our optimal point to perform strong coupling measurements (Fig. 11 (a)). A temperature increase moves the system into the weak coupling regime. This can be seen in Fig. 11 (b) and (c), where the pump power is the same as in (a), but the temperature is $T = 10$ K and $T = 19$ K, respectively. In these two cases, the avoided crossing is less significant than at 4 K. The ideal working will differ in a different material and type of device.

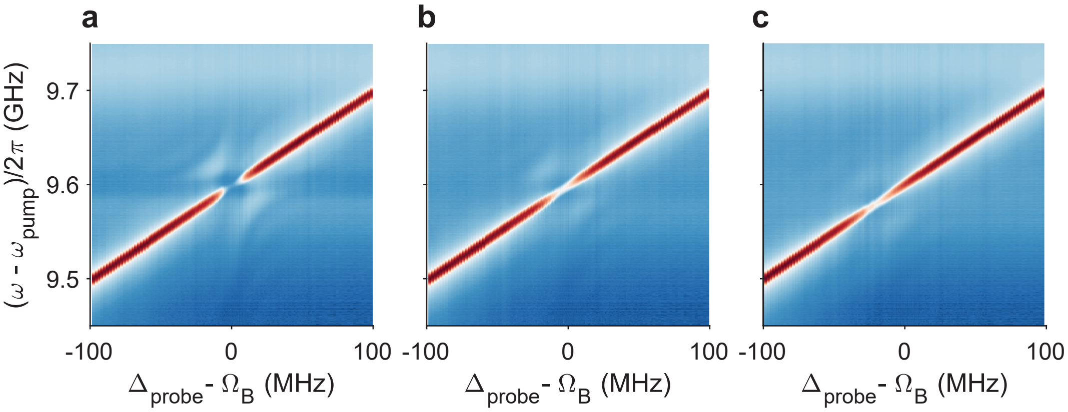

FIG. 11. **Temperature dependence of strong coupling regime.** (a) Forced detuning measurement at $T = 4$ K, $P_{pump} = 1.35 \pm 0.1$ W ($g_{om} = 70 \pm 2$ MHz). As the system is in the strong coupling regime, it shows a clear avoided crossing. (b) Forced detuning measurement for $T = 10$ K, same pump power as (a). The avoided crossing is not clearly visible, as the system enters the weak coupling regime. (c) Same as (b) with $T = 19$ K.

---

[1] A. Kobyakov, M. Sauer, and D. Chowdhury, Stimulated Brillouin scattering in optical fibers, Advances in Optics and Photonics **2**, 1 (2010).

[2] https://www.thorlabs.com/drawings/5e362a11bff048d-C6D1B9F8-FDBD-5B00-00D177E3E9204339/SMF-28-J9-SpecSheet.pdf.

[3] E. A. Cryer-Jenkins, A. C. Leung, H. Rathee, A. K. C. Tan, K. D. Major, and M. R. Vanner, Brillouin–Mandelstam scattering in telecommunications optical fiber at millikelvin temperatures, APL Photonics **10**, 010805 (2025).